Deep-Sea Research I 90 (2014) 48–61

Contents lists available at ScienceDirect

Deep-Sea Research I

journal homepage: www.elsevier.com/locate/dsri

Delving into three-dimensional structure of the West Luzon Eddy in a regional ocean model

Lei Wang [a,b], Jianping Gan [a,*]

[a] Department of Mathematics and Division of Environment, Hong Kong University of Science and Technology, Hong Kong, China
[b] State Key Laboratory of Tropical Oceanography, South China Sea Institute of Oceanology, Chinese Academy of Sciences, Guangzhou, China

ARTICLE INFO

Article history:
Received 25 October 2013
Received in revised form
9 March 2014
Accepted 15 April 2014
Available online 10 May 2014

Keywords:
Ocean Eddy
Dipole Eddy
Eddy Energy
Numerical modeling
West Luzon Eddy
South China Sea

ABSTRACT

The three-dimensional structure and associated dynamics of the prominent cold (cyclonic) West Luzon Eddy (WLE) were investigated by a high-resolution regional ocean model. The WLE was horizontally and vertically heterogeneous, exhibiting asymmetric structures in the circulation, vorticity, vertical motion and energy distributions within the eddy. The asymmetry was mainly attributed to the existence of an eddy dipole formed by a coexisting warm (anti-cyclonic) eddy to the south of the WLE. Analysis of the momentum balance revealed that the coexistence of two eddies intensified barotropic pressure gradients in the southern WLE to locally enhance the eastward jet. The positive (negative) vorticity of the jet strengthened (weakened) the eddy in the southern sector (periphery), which, together with the formation of a subsurface density front, intensified (suppressed) the corresponding upward motion and cooling. The baroclinic pressure gradients opposed the dominant barotropic components and spun down the eddy at greater depths with stronger weakening in the southern sector near the front. Asymmetric energy distributions showed that larger mean kinetic energy (MKE) and eddy available potential energy (EAPE) were stored in the southern sector of the WLE. While the larger MKE was directly linked with the stronger barotropic currents, the larger EAPE in the southern WLE was formed by baroclinic energy conversions due to a strong density gradient at the front.

1. Introduction

The South China Sea (SCS) is a marginal sea in Southeast Asia linked to the Pacific Ocean, East China Sea, Java Sea, and Sulu Sea by various straits. The upper layer circulation of the SCS is driven by seasonal monsoons. Using available historical data, Qu (2000) observed two cyclonic eddies as seasonally dominant features in the upper-layer circulation of the SCS: one located east of Vietnam called the East Vietnam Eddy and the other northwest of the Luzon Islands called the West Luzon Eddy (hereafter WLE) or the Luzon Cold Eddy. The WLE is situated at about 18°N, 118°E from late fall to early spring, coinciding well with a positive wind stress curl both in location and time (Qu, 2000). This eddy is one of the most important circulation features in the northern SCS and has also been well-identified in other investigations (e.g. Soong et al., 1995; Shaw et al., 1999; Liu et al., 2008).

The WLE corresponds to strong upwelling, a negative temperature anomaly in the subsurface, and a seasonal low sea level anomaly off Luzon in the northeastern SCS during the boreal winter. Shaw et al. (1996) referred to the WLE as a major upwelling region northwest of Luzon. This upwelling region was also reported by Udarbe-Walker and Villanoy (2001) and Martin and Villanoy (2007). Both Qu (2000) and Metzger (2003) noted the existence of a cyclonic eddy offshore of northwest Luzon during the winter and suggested its possible connection to the positive wind stress curl that prevailed there. Based on the results from numerical sensitivity experiments, Yang and Liu (2003) suggested that wind forcing controlled the generation of the WLE while the Kuroshio intrusion is of minor importance. Wang et al. (2008) proposed that the effects of wind stress curl, due to orographic wind jets, were a generation mechanism for the mesoscale eddies (including the WLE) in the eastern SCS.

Unraveling the three-dimensional structure of mesoscale eddies has been limited by the lack of observations and the complex dynamics of the system. Clarifying the three-dimensional structure and associated dynamics of the ocean's mesoscale eddies will help us understand the principle role that these eddies play in the dynamics of the ocean itself, considering that mesoscale eddies provide important dynamic fluxes for the equilibrium balances of the general circulation and climate (e.g. McWilliams, 2008) and material fluxes for the ventilation of heat, carbon and other biological elements (e.g., McGillicuddy et al., 1998, 2007; Chelton et al., 2011a).

The spatial structure of the ocean eddy is three-dimensional and its dynamics vary dramatically in horizontal and vertical directions. This three-dimensional structure greatly controls the

* Corresponding author.
E-mail address: magan@ust.hk (J. Gan).

http://dx.doi.org/10.1016/j.dsr.2014.04.011
0967-0637/

intensity, endurance, and dissipation of an eddy. For example, diapycnal mixing followed by geostrophic adjustment is considered to be the primary generation mechanism for sub-mesoscale coherent vortices in the ocean (McWilliams, 1985). Baroclinic structures and baroclinic instability have also been found to be important in regulating the evolution of many ocean eddies (e.g. Tabata, 1982; Babu et al., 1991; Badin et al., 2009; Kawaguchi et al., 2012). Satellite altimetry provides surface information only (e.g., Chelton et al., 2007; 2011b), and, although in situ measurements are able to provide some information on three-dimensional structures of ocean eddies (e.g., Johannessen et al., 1989; Flament et al., 1996; Hu et al., 2011), they are largely limited in time and space with difficulties to capture the full picture of the eddy for dynamic analysis. Most previous studies have taken the composite advantages of remotely sensed measurement and numerical models to unravel the three-dimensional eddy structure (e.g. Isern-Fontanet et al., 2004; Chaigneau et al., 2011; Dong et al., 2012; Yang et al., 2013; Zhang et al., 2013). However, the dynamic analysis of the three-dimensional structure for the ocean eddy has rarely been conducted. The three-dimensional structures of the WLE and its dynamic characteristics have not yet been explored. We lack understanding about the fundamental dynamic characteristics such as momentum, vorticity, and horizontal and vertical energy variation. In this study, we conducted an investigation of the three-dimensional structure of the WLE and its dynamic characteristics using a validated regional ocean model.

This paper is structured as follows: Section 2 presents the ocean model implementation and validations. Section 3 examines the three-dimensional hydrographic structure of the eddy including thermohaline characteristics, circulation, and energy distribution within the eddy using model results. Section 4 investigates the dynamic mechanisms for the formation of asymmetric structures within the eddy using the analyses of momentum balance and energy budget; and the summary and discussion are given in Section 5.

2. Ocean model

2.1. Model implementation

The Princeton Ocean Model (POM) (Blumberg and Mellor, 1987) is used in this study to solve three-dimensional, time-dependent, oceanographic flows. The model domain covers the whole SCS using a curvilinear horizontal grid (Fig. 1), with variable horizontal grid spacing from ~10 km in the northern and central parts of the domain to ~20–30 km in the eastern and southern parts. The total number of model grid points in the (x, y, σ) directions are (259, 181, 30), respectively. The bottom topography was from ETOPO2 (1/30°) from the National Geophysical Data Center. The initial conditions and lateral boundary conditions at the open boundary are from the Pacific Ocean Model (Curchitser et al., 2005). The surface wind stress and heat flux in the model are calculated using the National Centers for Environmental Prediction (NCEP) reanalysis data. The open boundary conditions developed by Gan and Allen (2005a) are utilized to represent the lateral momentum and buoyancy fluxes through the lateral open boundaries in the model.

The model was first spun up for 1500 days using a seven-year mean (1997–2003) surface and lateral forcing. After spin-up, the model was run in hindcast mode, forced with time-dependent, six-hourly surface forcing and three-day averaged lateral fluxes from 1 January 2000 to 30 June 2003. More detailed configurations and validations of the model can be found in Gan et al. (2006) and Gan and Qu (2008). We used model output from the last three years (July 2000–June 2003) for our analyses. Unless otherwise noted, the analysis results for the WLE in the following sections are calculated by averaging model results in November and December (2000, 2001, and 2002) and January (2001, 2002, and 2003), the period of which is called the peak WLE season hereafter.

2.2. Model validation

The capability of this model to reproduce the mesoscale circulation in the SCS region has been demonstrated in previous studies (Gan et al., 2006, Gan and Qu, 2008). Here, we present additional comparisons between available observations and the simulation results in the WLE region.

The first validation comes from comparisons of the spatial patterns of sea surface height anomalies (SSHAs) between observations and model results (Fig. 2). The observations of SSHAs are from a merged product of TOPEX/Poseidon (T/P), European Research Satellite (ERS) and Jason-1 satellites provided by the AVISO (Archiving, Validation, and Interpretation of Satellite Oceanographic Data). The observations (Fig. 2a) showed negative SSHAs, with values of about −0.1 m northwest of Luzon, coinciding with prevailing positive wind stress curls (contours in Fig. 2c). What is more, the observations also revealed positive SSHAs with values of about 0.05 m south of 15°N, corresponding to negative wind stress curls that were much weaker than the northern positive ones (Fig. 2c). The distribution of positive and negative wind stress curls west of Luzon was considered to be generated by isthmus wind jets associated with the islands' mountain ranges (Wang et al., 2008). The positive wind curls, generated by the shielding effects of the northeast monsoon due to the Luzon Islands, were considered to be the main forcing factor for the WLE formation (e.g., Yang and Liu, 2003; Wang et al., 2008). Consistent with the observed SSHAs, a cyclonic circulation, i.e. the WLE, was found north of 15°N, and another anti-cyclonic circulation was observed south of 15°N in the AVISO geostrophic current fields (Fig. 2a). Apparently, the cold cyclonic WLE and the warm anti-cyclonic eddy formed an eddy dipole. As a result, the southern sector of the WLE was largely regulated by the effect of the dipole and tended to have a strong surface current. These observed features were well-captured by the model. The simulated patterns of SSHAs and geostrophic velocities resembled those from the observations, despite the model's having overestimated the SSHAs in the area close to the Luzon Islands (Fig. 2b). The core of the WLE in the model results shifted slightly eastward (Fig. 2b) and extended farther northeastward in its northern sector. The differences between the model and observation may be ascribed to many reasons, but likely associated with the inaccuracies of wind forcing and topography.

The second validation is for a comparison of temporal variations of the sea surface temperature (SST) and SSHAs in the WLE region (Fig. 3). The observed SSTs were from the Moderate Resolution Imaging Spectroradiometer (MODIS) satellite. From the observations, it can be seen that both SSTs and SSHAs in the WLE region underwent significant seasonal variations. SSTs peaked at values exceeding 28 °C from May to October and they reached values below 25 °C from January to March. Negative SSHAs, with values less than −0.1 m, were present from November to February, and positive SSHAs, with values exceeding 0.1 m, were found from July to October. The simulated results compared well with the corresponding seasonal variations in the observed fields. The high correlation between the simulations and observations demonstrated that the model had considerable skill in reproducing hydrodynamic features in the WLE region.

Overall, the above comparisons, as well as the validations provided in Gan et al. (2006), showed the similarities between simulated results and observations and established a level of confidence in the model.

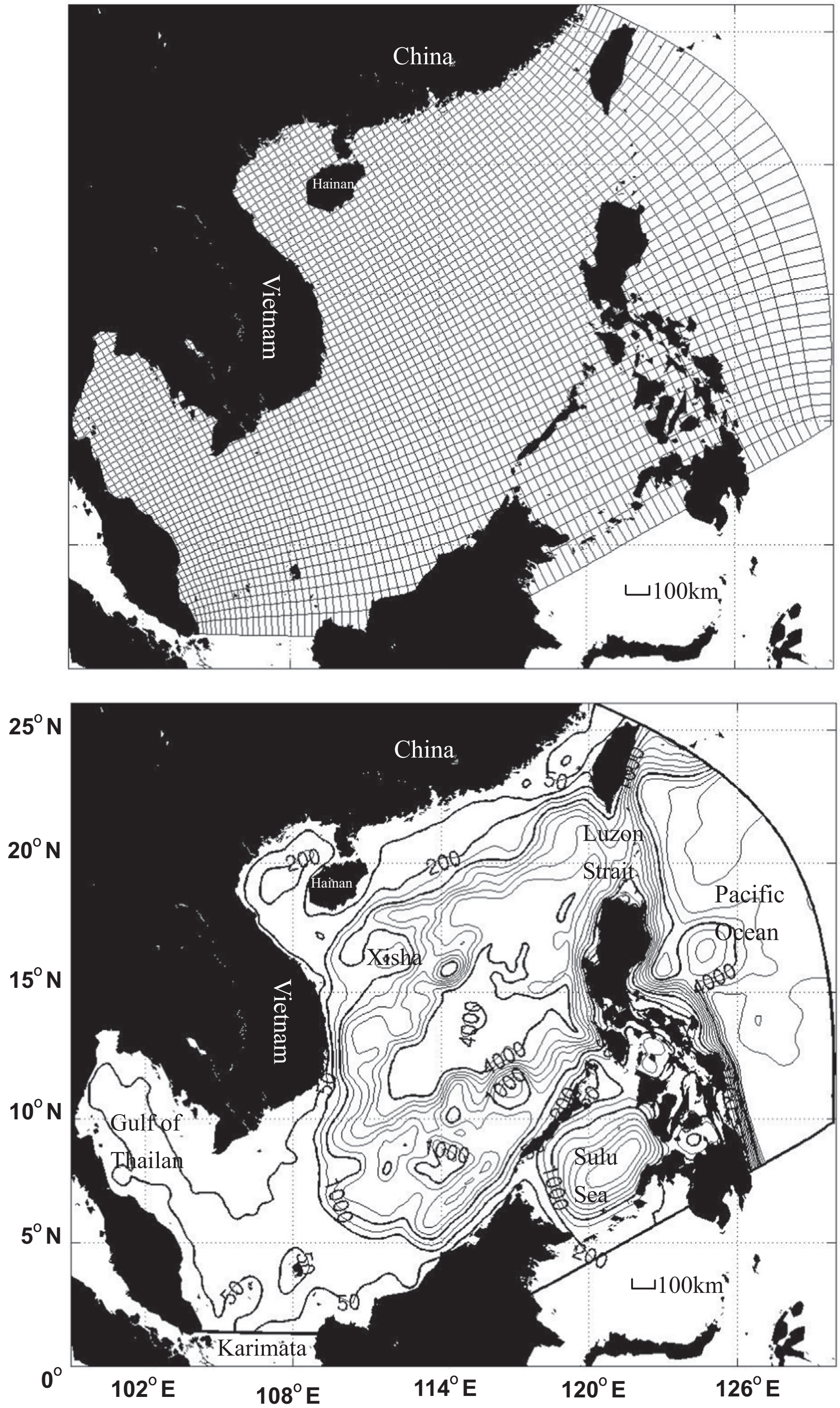

Fig. 1. The model's curvilinear grid and bathymetry with the 50, 200, 1000 and 4000 m isobaths shown as thicker lines. The contour interval for water deeper than 200 m is 500 m. One-third of the horizontal grid point is shown.

3. Hydrographic structure of the West Luzon Eddy

In this section, we present the simulated three-dimensional hydrographic structure of the WLE, including thermohaline characteristics, circulation, and the energy distribution.

3.1. Thermohaline characteristics of the eddy

The simulated temperature and salinity distributions in the WLE region are presented in Fig. 4 for different depths. At the surface, there was nearly homogeneous warm water (Fig. 4a) and the cold core of the eddy was invisible, suggesting that the temperature signals associated with the eddy were not significant in the surface layer. The surface signal of the eddy may have been damped by air–sea interaction and surface heat fluxes as suggested by Hu et al. (2011). At 20 m, an isotherm with temperature < 22 °C enclosed the cold core (Fig. 4b). The temperature signal of the cold eddy can be clearly recognized at 50 m with the lowest temperature, < 18 °C, centered at around 118°E and 17°N (Fig. 4c). The horizontal temperature gradients were near their maxima at

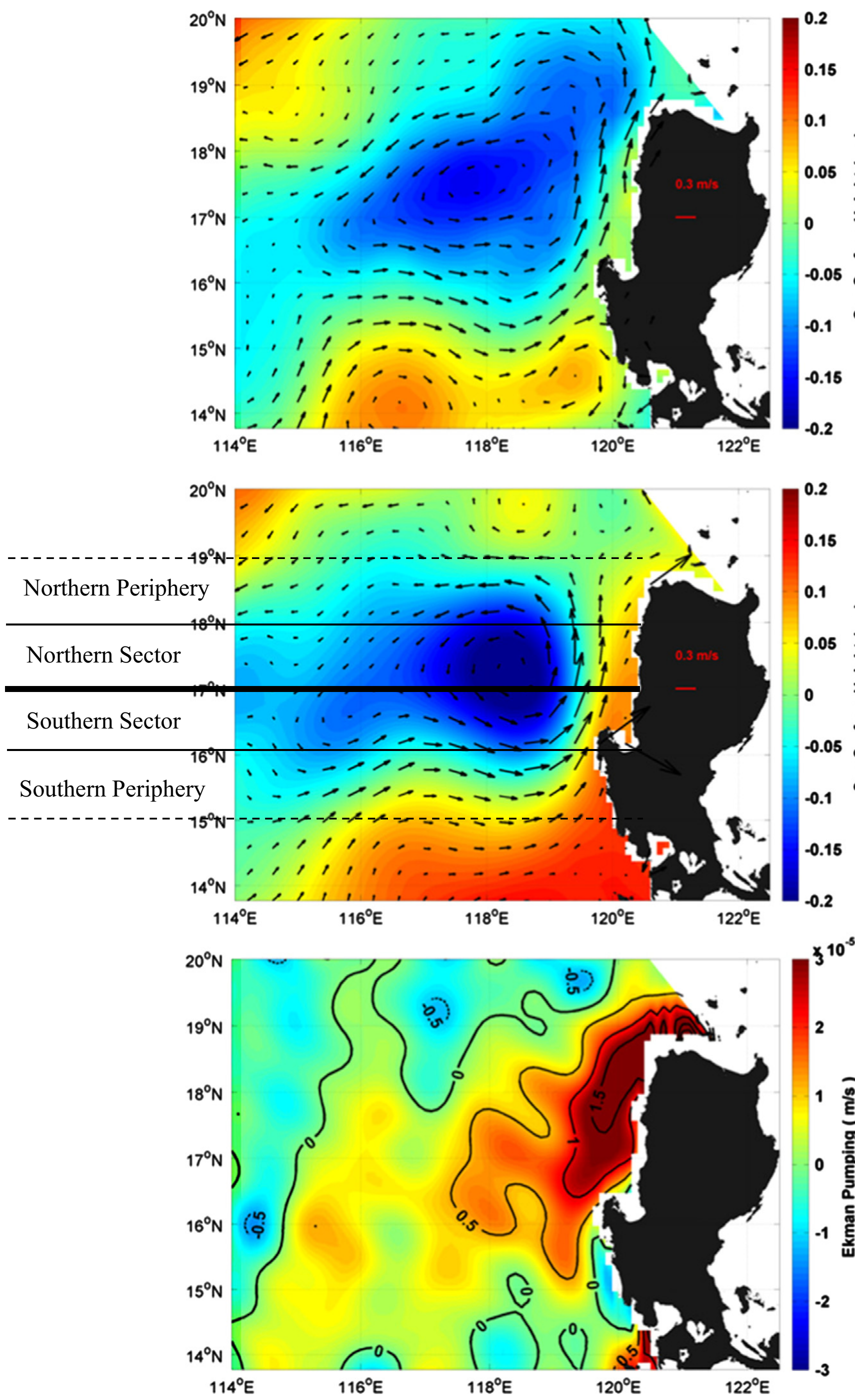

Fig. 2. (a) Satellite observed SSHA (m, shading) and geostrophic velocity vectors; (b) modeled SSHA (m, shading) and geostrophic velocity vectors. Spatial division of the eddy is also displayed; (c) wind stress curl (10^{-6} N m^{-3}, black contours) and Ekman pumping velocity (10^{-5} m s^{-1}, shading). All values are averaged in the peak WLE season.

50 m, the magnitudes of which reached to around 0.05 °C km^{-1} along the southern and eastern flanks of the cold core. Similar eddy-like isotherm distributions could also be found at 75 m and 100 m,with the lowest temperature of ~16 °C at 75 m (Fig. 4d) and < 15 °C at 100 m (Fig. 4e). The temperature in the core of the eddy decreased with increasing depth and reached to < 12 °C at 150 m (Fig. 4f). Until 200 m, the horizontal temperature gradients were decreased and the cold core of the eddy gradually dissipated (Fig. 4g). Beneath 200 m, the cold core nearly disappeared (Fig. 4h and i). The temperature signal of the cold eddy was mainly a subsurface feature and was most significant between 50 m and 200 m where the pycnocline existed. Although, beneath 200 m, the temperature signal of the cold eddy was not significant, the cyclonic circulation associated with the eddy could penetrate to and be visible until 500 m (also see Fig. 6 below). These depth-dependent features are very similar to those seen in recent *in situ* measurements (Hu et al., 2011).

The vertical distribution of the temperature field and temperature anomalies along the 118°E transect crossed the eddy center are also illustrated in Fig. 5. The temperature anomaly was obtained by subtracting the mean reference temperature profile from each individual temperature profiles. The mean reference

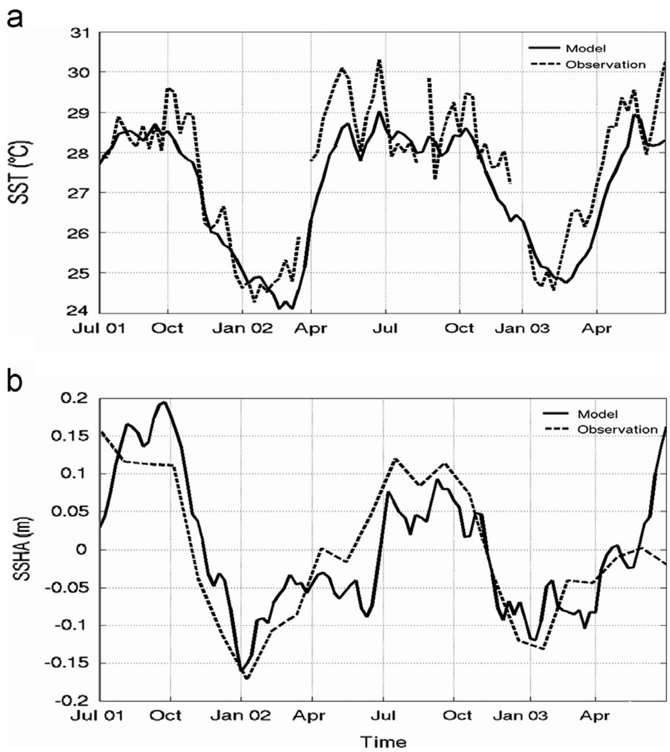

Fig. 3. Comparison of time series for modeled (solid lines) and observed (dashed lines) (a) sea surface temperature (°C) and (b) SSHA (m) averaged between 116.35° and 119.65°E across 16°–18°N where the WLE was located. The dashed line in (a) is broken near April 2002 and January 2003 due to the deficiency and unavailability of satellite observations.

temperature profile at one latitude is calculated by averaging the temperature profiles at grid points outside the eddy between 114°E and 120°E. The presence of the eddy was manifested by the lift of the isotherms and was depicted by a well-developed dome of isotherms. The isotherms had vertical displacements reaching several tens of meters, with the maximum lift located around the eddy center at ~17°N. Temperatures at the center of the eddy were 2–3 °C lower than those on the periphery. The temperature anomaly section illustrated the existence of a cold eddy core enclosed by the −1.5 °C anomaly. South of 15°N, a warm core was observed with the temperature anomaly larger than 1.0 °C at ~50–200 m, which was considered to be associated with the anticyclonic warm eddy due to the local negative wind stress curls (Fig. 2). The coexistence of the cold and warm eddies generated the eddy dipole and a strong subsurface temperature front at depths of ~50–100 m. The front could have led to a velocity shear in vertical direction because of the thermal wind relation so that the velocity beneath it would be reduced.

Similar to the isotherms, the rising isohalines and salinity anomalies in the vertical salinity distribution also indicates the presence of the eddy (Fig. 4c and Fig. 5b). At the center of the cold eddy, salinities were 0.1–0.2 higher than in the ambient water. The isohalines had vertical displacements of several tens of meters with maximum uplift at the eddy center, around 17°N. Negative salinity anomalies with values of ~−0.05 at ~50–100 m were observed for the warm eddy south of 15°N (Fig. 5b).

3.2. Circulation of the eddy

The simulated three-dimensional structure of the ocean currents and vorticity for the WLE are presented in Fig. 6. Under forcing from the positive wind stress curl (Fig. 2), a closed cyclonic ocean circulation was observed from the surface to a depth of ~500 m over which the magnitude of ocean currents decreased from ~0.3 m s^{-1} to <0.1 m s^{-1}. The magnitude of vorticity decreased sharply from the surface to the deeper ocean layers, with values of 1.0×10^{-5} s^{-1} at the surface and $<0.3\times10^{-5}$ s^{-1} at 500 m, indicating that the upper part of the eddy was effected by the positive vorticity from wind stress curls.

The spatial scale of the ocean eddy can be determined by the Okubo–Weiss parameter, W (Isern-Fontanet et al., 2004; Gan and Ho, 2008):

$$W = s_n^2 + s_s^2 - \omega^2, \tag{1}$$

where the vorticity (ω) and the normal (s_n) and shear (s_s) components of the strain are defined, respectively, as

$$\omega = \frac{\partial v}{\partial x} - \frac{\partial u}{\partial y}, s_n = \frac{\partial u}{\partial x} - \frac{\partial v}{\partial y}, s_s = \frac{\partial v}{\partial x} + \frac{\partial u}{\partial y}, \tag{2}$$

here, u and v are horizontal velocity components. The eddy core is usually defined as a coherent region of negative W, using a threshold value of $-0.2\sigma_W$, where σ_W is the standard deviation of W.

We used the Okubo–Weiss parameter in Eq. (1) to define the spatial scale of the core area in the eddy. The eddy core radius, R, is then defined by $=\sqrt{A/\pi}$, where A is an area encircled by the $-0.2\sigma_W$ contour. As shown in Fig. 6, by the $-0.2\sigma_W$ contour (Isern-Fontanet et al., 2004), the eddy's core size was largest at the surface, with R~60 km. It decreased gradually with increasing depth and became <30 km below 200 m. The baroclinicity may spin down the WLE in the greater depth, as to be shown in the analysis below.

The vertical distribution of the zonal component of velocity (u) across the eddy, along 118.0°E, is presented in Fig. 7a. The contour line of zero velocity was observed near the eddy center at ~17°N. In the southern sector (south of 17°N, also see Fig. 2), an eastward current was baroclinically sheared, decreasing from 25 cm s^{-1} at the surface to 10 cm s^{-1} at 200 m, which was likely associated with the horizontal temperature gradients in the eddy (Fig. 5) due to the thermal wind relation. The maximum surface zonal velocity was located at 15.6°N at the southern flank, about 140 km away from the eddy center. In the northern sector (north of 17°N), a westward current >10 cm s^{-1} occupied the water column from the surface to a depth of 120 m.

The zonal velocity along the south–north transect was largely asymmetric. The southern sector of the eddy had a stronger current intensity, deeper vertical extension, and larger radius compared with the northern sector. The magnitude of the zonal velocity in the southern sector tended to be 10 cm s^{-1} stronger than that in the northern sector at the same water depth. Larger vertical extension existed in the southern sector of the eddy. The maximum current radius (MCR) (defined as the distance between the surface maximum velocity and the eddy center) was about 40 km larger in the southern sector than in the northern sector. Corresponding asymmetry was also found in the vertical distribution of relative vorticity crossing the eddy center (Fig. 7a). Positive vorticities were observed from the eddy center to within the MCR, and they became negative outside the MCR in the peripheries. Consistent with stronger horizontal velocity shear and intensity in the currents, there were also stronger positive vorticities in the southern sector compared with the northern part.

Vertical motion in the upper ocean is instrumental in supplying heat, salt, and momentum fluxes for the eddy. Fig. 7b presents the vertical distribution of the vertical velocity along 118.0°E. The signal of vertical velocity in the WLE can penetrate to more than 500 m. The eddy was dominated by upward vertical velocities between 16°N and 18°N across the northern and southern sectors. The intensity of the upward motion, however, was much stronger in the southern sector. Another patch of relatively strong upward

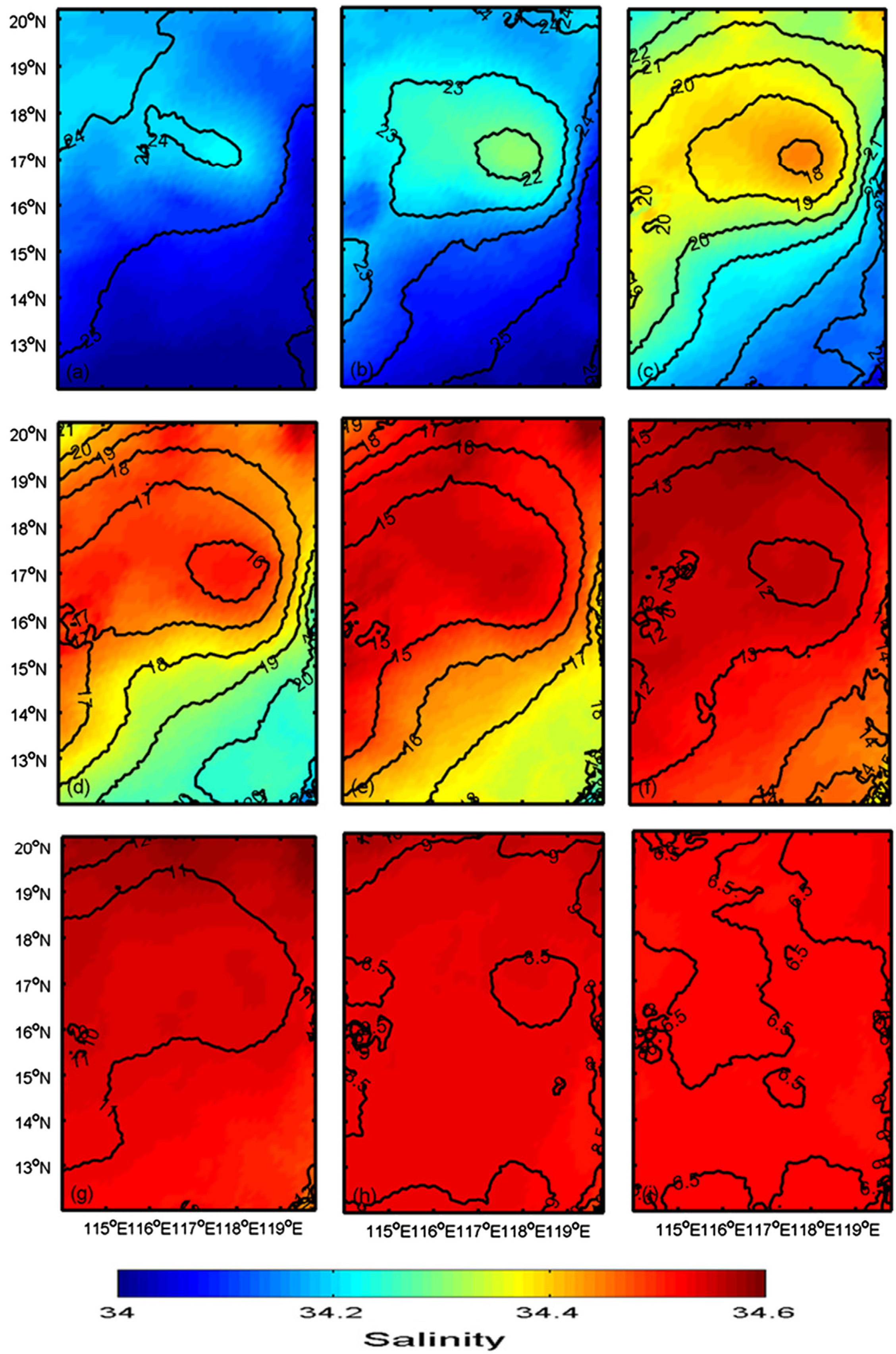

Fig. 4. Temperature (°C, black contours) and salinity (shading) distributions in the West Luzon Eddy region at nine levels: (a) surface, (b) 20 m, (c) 50 m, (d) 75 m, (e) 100 m, (f) 150 m, (g) 200 m, (h) 300 m, and (i) 500 m.

vertical velocities was observed between 18°N and 19°N in the northern periphery of the eddy (Fig. 2b). Downward vertical velocities were found south of 16°N at the southern periphery of the eddy. While the positive vorticity (Fig. 7a) was linked with

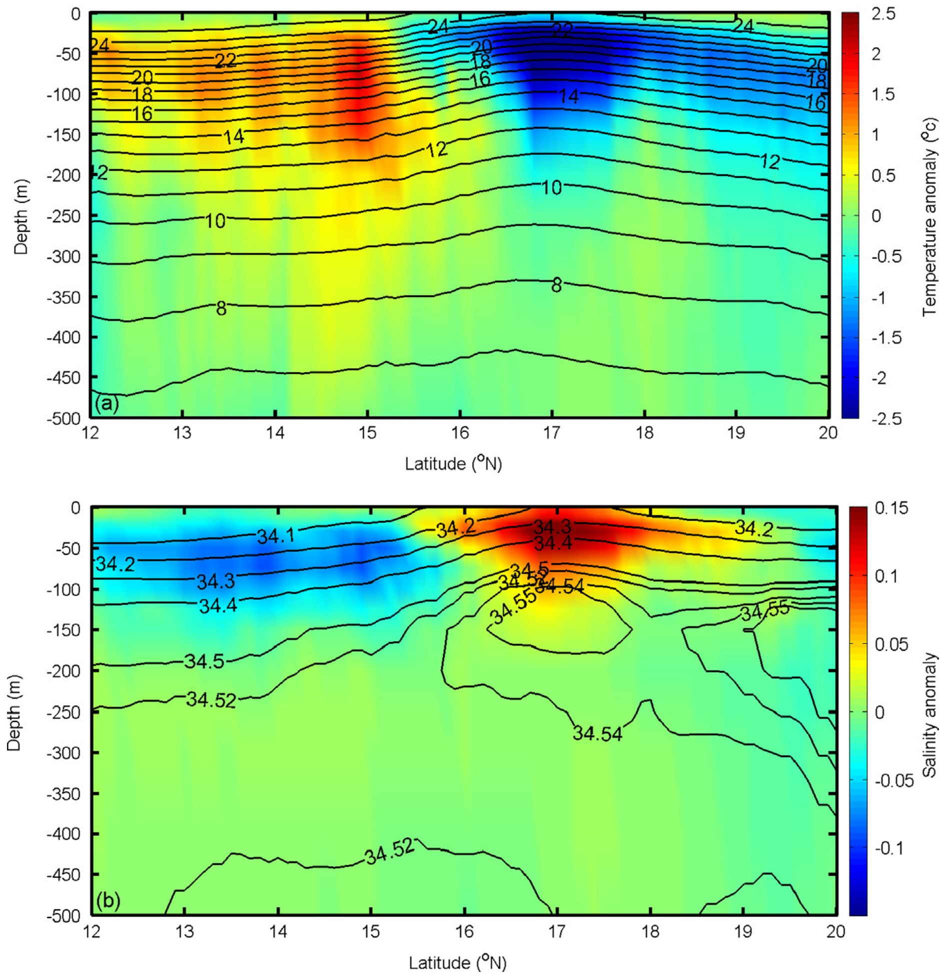

Fig. 5. Vertical distribution of (a) temperature (°C, black contours) and temperature anomaly (°C shadings). (b) Salinity (contours) and salinity anomaly (shadings) across the eddy along 118.0°E from the model results.

upward velocities between 16°N and 18°N, the negative vorticities were attributed to both upward and downward vertical velocities in the northern and the southern peripheries, respectively. Obviously, the vorticity was not the dominant factor in the northern periphery.

The temperature and salinity anomalies (Fig. 5) correlated well with the variation of vertical velocity along section 118°N (Fig. 7b). Negative temperature and positive salinity anomalies in the northern sector were linked with the two patches of the relative large upward vertical velocities in this location. The stronger vertical velocities were found in the depths >200 m likely due to the enhanced convergence in the ageostrophic flow (e.g. Mahadevan and Tandon, 2006). However, larger values of the temperature and salinity anomalies located in the thermocline/halocline in the depths <100 m, as a result of larger vertical gradients. In addition, the lifting and sinking motions at the southern sector and southern periphery of the eddy intensified the meridional gradients of the isotherms, isohalines, and isopycnals (Fig. 5) and thus the barocinlic pressure gradients as shown below.

The model results show that the vertical circulation around the eddy is more complex than the standard conceptual models of upwelling at the center of a cold-core eddy (e.g. Lee et al., 1991; McGillicuddy et al., 1998). Besides upwelling at the center of the cold-core eddy, downwelling occurred in the southern periphery and an additional upwelling existed in the northern periphery (Fig. 7b). Qualitatively similar vertical velocity distributions have been inferred from observations of the Gulf Stream (Osgood et al., 1987) and the Brazil Current (Campos et al., 2000). In both cases, estimates of vertical velocity fields associated with poleward propagating cold-core eddies have noted upwelling at the leading edge of the eddy and downwelling at the trailing edge, due to divergence on the leading edge of the dome and convergence on its trailing edge. Oke and Griffin (2011) also revealed that the circulation around a cyclonic eddy off the coast of New South Wales in early 2007 was ageostrophic, with upwelling in the southern sector and downwelling in the northern sector. Hu et al. (2011) showed that besides upward velocities around the center of a cold eddy in the southeastern SCS, there were downward velocities to the southwest and to the east of the center, which might have been triggered by vertical turbulent flux and baroclinic instability. All these previous studies suggested that upwelling and downwelling coexisted in a cold eddy just as they do in our model results for the WLE, although the detailed forcing mechanisms may vary from different ocean eddies and from different geographic regions.

The wind stress curl may be one of the reasons for the generation of vertical motions due to the Ekman pumping effects (Fig. 2c). The wind stress curl became negative south of 15°N and the Ekman pumping velocities were also negative due to negative wind stress curls (Fig. 2c). However, this cannot explain the downward vertical velocities between 15°N and 16°N around the perimeter where wind stress curls were positive. In addition to the local Ekman pumping, the westward propagation of

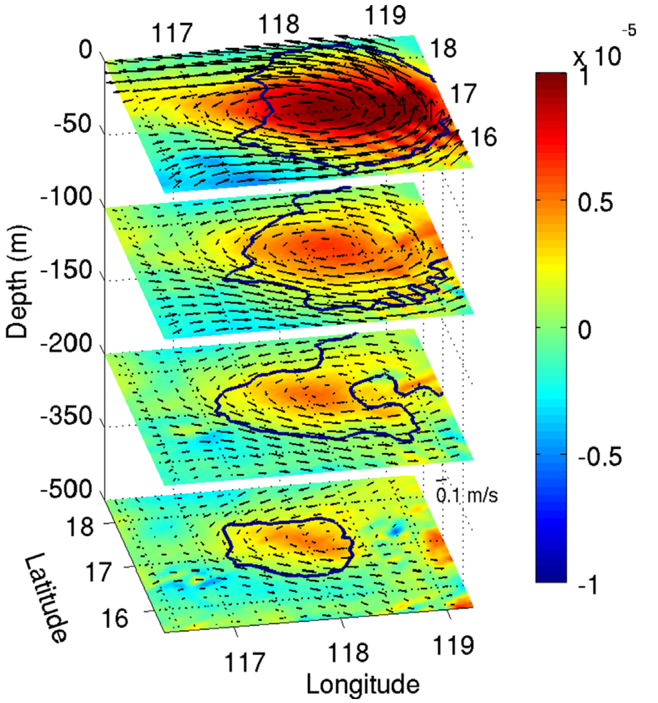

Fig. 6. Velocity vectors (m s^{-1}) and vorticity (10^{-5} s^{-1}) at depths of 0 m, 100 m, 200 m, and 500 m. Contour lines are $W = -0.2\sigma_w$ at each depth.

upwelling/downwelling Rossby waves may also modulate the vertical motions within the eddy, although their magnitudes are expected to be less significant in this region. It is also noted that baroclinic frontal structure between the warm and cold eddies in the dipole may modulate geostrophy to form ageostrohphic secondary circulation and vertical motion (e.g. Mahadevan and Tandon, 2006; also see the momentum analysis below) in the flow. The complex vertical motion in the WLE may be formed by horizontal strain, convergence, and baroclinic instabilities in the ageostrophic flow, and the detailed forcing mechanism for the vertical motion requires a comprehensive study in a separate investigation.

3.3. Energy of the eddy

Rotating flow associated with ocean eddies is characterized by the presence of long-lived concentrations of vorticity and energy. Rotating fluids adjust to a geostrophic balance rather than to a state of rest. This state of equilibrium may be characterized by potential energy that is available for conversion to other forms of energy (Gill, 1982). The available potential energy per unit mass in a volume element, V, is approximated by (e.g., Oort et al., 1989)

$$P = -\frac{1}{2} g \iiint \frac{(\rho - \rho_0)^2}{\rho_0 d\rho_0/dz} dV, \tag{3}$$

where, ρ is potential density, and $\rho_0(z)$ is the reference potential density that is horizontally averaged over the time-mean potential density distribution. Neglecting the contribution of vertical velocity, the kinetic energy per unit mass is given by

$$K = \frac{1}{2} \iiint (u^2 + v^2) dV, \tag{4}$$

where u and v are horizontal velocity components.

Separating the actual variables into time mean and transient parts ($u = \overline{u} + u'$, $v = \overline{v} + v'$, $\rho = \overline{\rho} + \rho'$), the time-mean energy of the system may be divided into four components of mean available potential energy (MAPE, P_m)

$$-\frac{1}{2} g \iiint \frac{(\overline{\rho} - \rho_0)^2}{\rho_0 d\rho_0/dz} dV, \tag{5}$$

eddy available potential energy (EAPE, P_e)

$$-\frac{1}{2} g \iiint \frac{(\rho'^2)}{\rho_0 d\rho_0/dz} dV, \tag{6}$$

mean kinetic energy (MKE, K_m)

$$\frac{1}{2} \iiint (\overline{u}^2 + \overline{v}^2) dV, \tag{7}$$

and eddy kinetic energy (EKE, K_e)

$$\frac{1}{2} \iiint (\overline{u'^2 + v'^2}) dV. \tag{8}$$

The vertical distributions of the four energy components within the eddy are presented in Fig. 8. Asymmetric structures were also observed for energy distributions within the eddy. The distribution of MKE (Fig. 8a) was consistent with the one in ocean currents (Fig. 7a) and had a larger MKE in the southern sector due to stronger ocean currents there. Large values of MAPE were observed around the eddy center at 17°N above 200 m (Fig. 8b), as a result of the lifting isopycnals (Fig. 5). The MAPE was largely a measure of the thermocline slope within the eddy. High values of MAPE also existed between 14°N and 15°N (Fig. 8b), which is consistent with the steeper thermocline there compared to the relatively flat thermocline in the northern part (Fig. 5). For the EKE, the northern sector had larger values of EKE than in the south (Fig. 8a). Opposite patterns were found for the EAPE, with larger values in the south and smaller magnitudes in the northern sector (Fig. 8b). Analysis of the energy conversions and the associated physical explanation will be conducted in Section 4.2 to gain more insight into the dynamics that attributed to the asymmetric WLE.

4. Dynamics of the West Luzon Eddy

In this section, we will apply momentum and energy budget analysis to explain the asymmetric structures of the ocean current and energy within the WLE. The analysis intends to explain why the ocean currents and EAPE are stronger in the southern sector of the eddy than in the northern sector.

4.1. Momentum budget

Dynamical processes involved in the forced flow fields are investigated by examining the momentum budgets in order to shed some light on the dynamics. The depth-dependent momentum equations can be written as

$$\overbrace{\frac{\partial u_i D}{\partial t}}^{(1)} + \overbrace{\sum_{j=1,2} \frac{\partial u_i u_j D}{\partial x_j} + \frac{\partial u_i \omega D}{\partial \sigma} - F_i D}^{(2)} + \overbrace{(-1)^i f u_i D}^{(3)} - \overbrace{\frac{\partial}{\partial \sigma}\left(\frac{K_M}{D}\frac{\partial u_i}{\partial \sigma}\right)}^{(4)}$$
$$+ \overbrace{gD\frac{\partial \eta}{\partial x_i} + \frac{gD^2}{\rho_0}\int_\sigma^0 \left(D\frac{\partial \rho'}{\partial x_i} - \frac{\sigma'}{D}\frac{\partial D}{\partial x_i}\frac{\partial \rho'}{\partial \sigma'}\right) d\sigma'}^{(5)} = 0, \tag{9}$$

where the momentum equations are rotated from model curvilinear coordinates to be directed in the east–west (x) and north–south (y) directions, represented by subscripts $i = 1$ and 2 in the variables, respectively. $D = H + \eta$ (H is bottom topography and η is surface elevation); ω is the vertical velocity using σ coordinates; F_i is the horizontal viscosity term; K_M is the vertical turbulent viscosity coefficient; and ρ_0 and ρ' are the reference density and density anomaly. Terms in Eq. (9) are normalized by D and referred to as the (1) acceleration, (2) nonlinear advection and diffusion (NL),

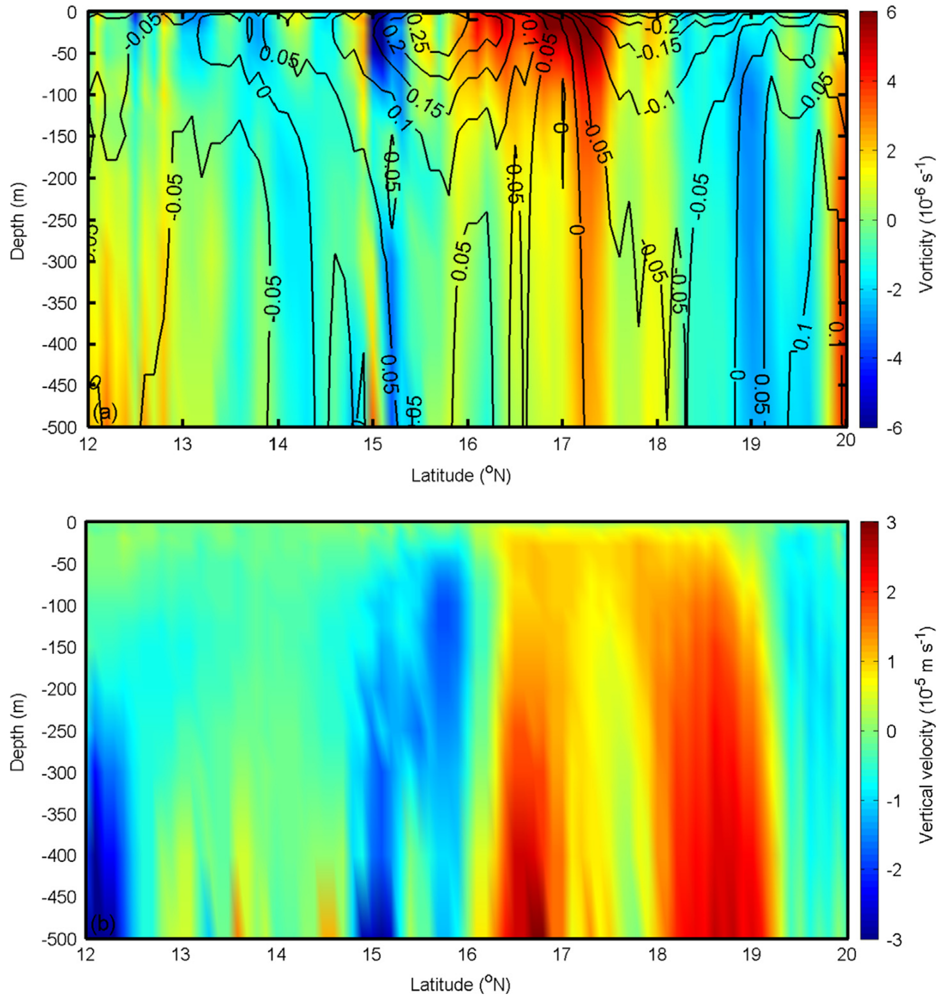

Fig. 7. Vertical distribution of (a) zonal component of velocity (m s, black contours) and vorticity (10^{-6} s^{-1}, shading) and (b) vertical velocity (10^{-5} m s^{-1}, shading) across the eddy along 118.0°E.

(3) Coriolis force (COR), (4) vertical viscous term (DIFF), and (5) pressure gradient (PRE). The pressure gradient consists of two parts: barotropic pressure gradient (BTPG) and baroclinic pressure gradient (BCPG). The BTPG is associated with the horizontal changes of surface elevation while the BCPG is caused by horizontal changes in density. It is also convenient to consider the behavior of the sum of COR and PRE, which is referred to as the ageostrophic term (AGE) or ageostrophic pressure gradient force (Gan and Allen, 2005b).

The momentum budgets in the north–south direction along 118.0°E are shown in Fig. 9. Positive and negative values of COR, representing the eastward and westward currents, existed in the southern and northern sectors of the eddy, respectively. COR was mainly balanced by PRE, suggesting that the circulation in the eddy was generally dominated by the geostrophic balance. The magnitude of AGE was one order smaller than COR and PRE, but may play a significant role in eddy dynamics (Hoskins and Bretherton, 1972; McWilliams, 1985). Near the surface, negative AGE was found in both southern and northern sectors, provided by the net contribution of local negative PRE in the southern sector and local negative COR in the northern sector. This negative AGE near the surface was balanced by positive DIFF due to the effects of surface wind stress. Positive values of DIFF near the surface reflected the response to the wind stress of the turbulent boundary layer (~15 m depth). Beneath 10 m, negative values of AGE were found in the southern sector and positive values in the northern sector, both signals of which penetrated to ~200 m depth. A similar pattern and magnitude of NL, with opposite sign at the same location, suggested that AGE was balanced by NL between 10 m and 200 m. NL included the effect of centripetal acceleration due to the curvature associated with cyclonic circulation within the eddy.

Overall, the magnitudes of momentum terms showed strong horizontal asymmetry within the eddy. In addition, the vertical variations of terms indicated that the WLE was highly variable with depth. Besides the effects of horizontal asymmetry (Fig. 2c) and variable vertical extent of the wind forcing, frontal dynamics associated in the dipole south of the WLE (Fig. 2) shape this three-dimensional structure.

The horizontal changes in surface elevation and density can separately generate BTPG and BCPG. The SSHA along 118°E is presented in Fig. 12a. The cyclonic eddy had a minimum SSHA close to −14 cm at the eddy center around 17.2°N. The SSHA tended to increase from the eddy center to the periphery. The horizontal changes in sea surface height generated BTPG that drove the cyclonic circulation within the eddy.

Both modeled results and altimetry measurements showed much stronger gradients of SSHAs in the southern part of the eddy than in the northern part. From 17°N to 15°N, the SSHA increased from −14 cm to 7 cm. The increase of the SSHA south of 15°N was mainly due to the existence of an anti-cyclonic eddy.

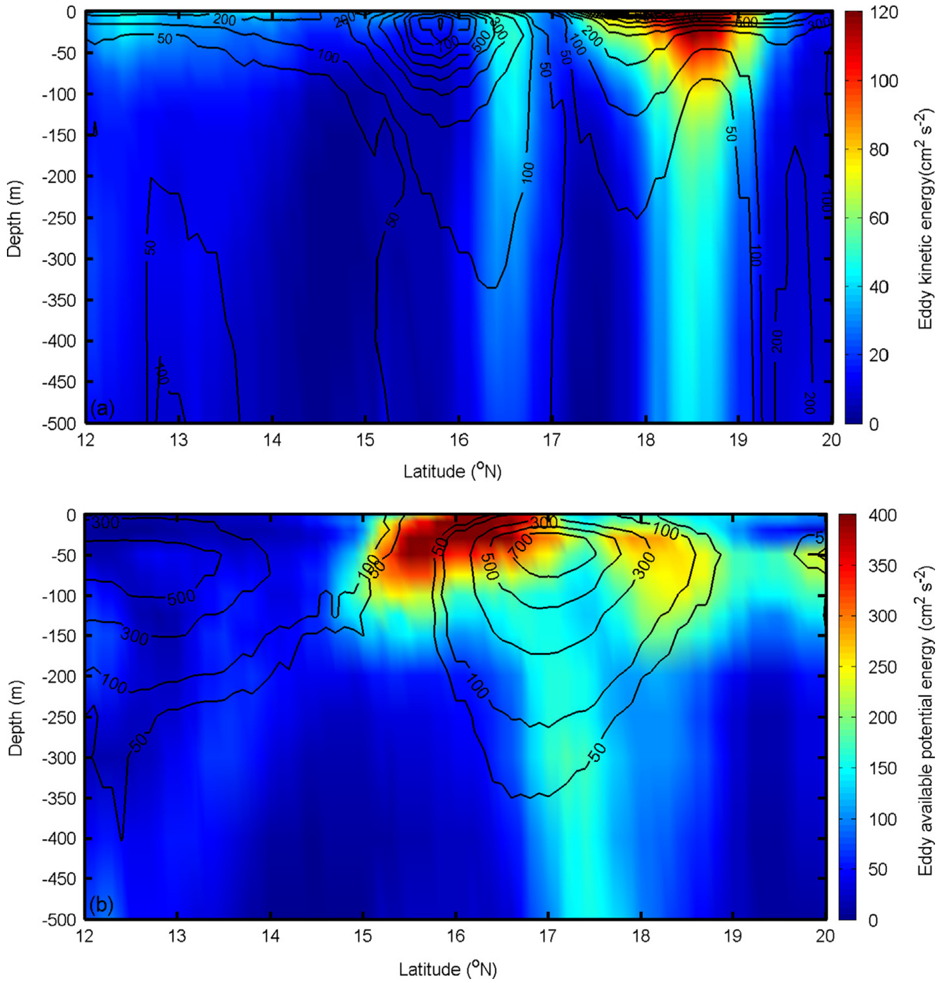

Fig. 8. Vertical distribution of (a) MKE (cm^{-2} s^{-2}, black contours) and EKE (cm^{-2} s^{-2}, shading) and (b) MAPE (cm^{-2} s, black contours) and EAPE (cm^{-2} s^{-2}, shading) across the eddy along 118.0°E.

While in the northern part of the eddy, the SSHA increased from -14 cm at 17°N to ~ -4 cm at 19°N. The source of horizontal gradient of SSHA is mainly set up by the divergence through Ekman pumping of wind stress curl, but it cannot account for the asymmetric SSHA gradients in the southern periphery between 15°N and 16°N where wind stress and wind stress curls were relatively weak (Fig. 2c). The coexistence of the WLE and the warm eddy produced 1.7 times larger sea surface height gradients and much stronger BTPG in the southern part of the WLE than in the northern part. In the upper 200 m, the total pressure gradient was mainly governed by the BTPG arising from the horizontal gradient of SSHA (Fig. 9).

It is informative to look into the asymmetric effect of the baroclinic component of the pressure gradient that arises from the horizontal gradient of density (Fig. 9d). BCPG had larger magnitudes in the southern sector than in the north, as a result of the density front in the eddy dipole (Fig. 10b). The frontal effect also increased the nonlinearity and, thus, the ageostrophy in the southern sector (Fig. 9f). The positive/negative ageostrophy may also affect the intensity of vertical motion below surface of the northern and southern parts of the eddy (Fig. 7b), as a result of changing strain and divergence in the flow field (Mahadevan and Tandon, 2006).

The magnitude of the BCPG increased with depth and its sign opposed total PRE. The BCPG, thus, worked to spin down the cyclonic circulation that was mainly set up by the BTPG and by a core of high density water in the eddy. Strong BCPG below 200 m limited the vertical extension of the eddy being mainly within the upper 200 m. Similarly, the BCPG tends to have a strong spinning-down effect in the southern sector of the eddy.

Apparently, the coexistence of the WLE and the adjacent warm eddy largely shaped the asymmetry of the WLE; it also modulated horizontal and vertical intensity of baroclinicity within the WLE to strengthen the asymmetry.

4.2. Energy budget

To gain more insight into the dynamic processes of the asymmetric WLE, we further examined the asymmetry based on energy conversion. Following Boning and Budich (1992) and Brown and Fedorov (2010), the four-box energy transfer (Lorenz, 1955), per unit mass, in a volume element, V, is given by

$$T_1 = \iiint \overline{(\rho-\rho_0)}\,\overline{w} g/\rho_0 dV, \tag{10}$$

$$T_2 = -\iiint g\frac{\left(\overline{u'\rho'}\frac{\partial\overline{\rho}}{\partial x}+\overline{v'\rho'}\frac{\partial\overline{\rho}}{\partial y}\right)}{\rho_0\frac{d\rho_0}{dz}}dV, \tag{11}$$

$$T_3 = \iiint g\overline{\rho' w'}/\rho_0 dV, \tag{12}$$

$$T_4 = -\iiint\left\{\overline{u'u'}\frac{\partial\overline{u}}{\partial x}+\overline{u'v'}\left(\frac{\partial\overline{v}}{\partial x}+\frac{\partial\overline{u}}{\partial y}\right)+\overline{v'v'}\frac{\partial\overline{v}}{\partial y}\right\}dV, \tag{13}$$

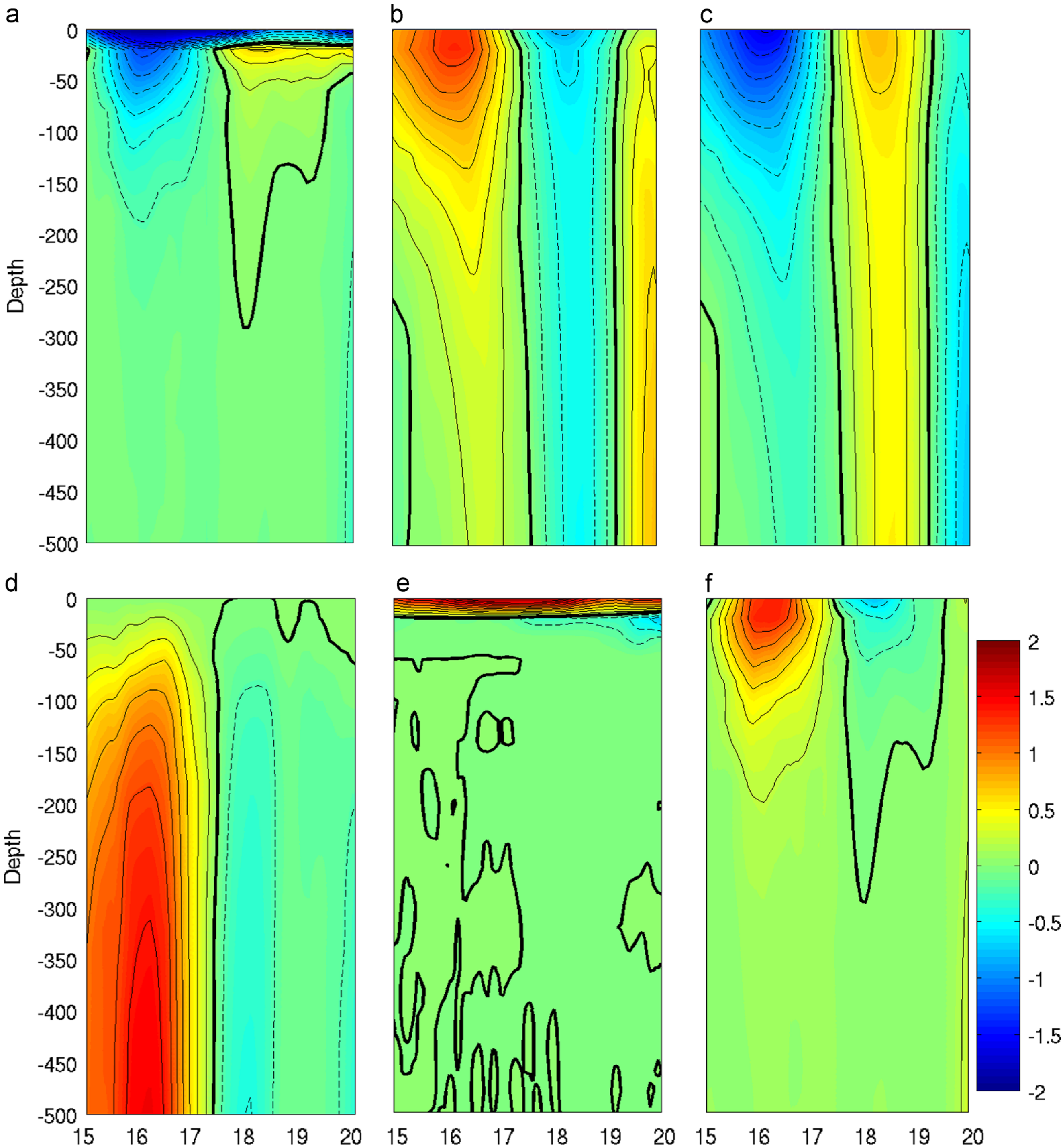

Fig. 9. Cross sections of (a) ageostrophic pressure gradient (in m s^{-2}, multiplied by 10^6), (b) Coriolis term (multiplied by 10^5), (c) total pressure gradient (multiplied by 10^5), (d) baroclinic pressure gradient (multiplied by 10^5), (e) viscosity (multiplied by 10^6), and (f) nonlinear advection (multiplied by 10^6) of N–S direction momentum term balance along line 118.0°E.

where T_1 represents the conversion of MKE to MAPE ($K_m \rightarrow P_m$) by the work of the mean buoyancy forces; T_2 is the transfer of MAPE to EAPE ($P_m \rightarrow P_e$), usually through baroclinic instabilities of the mean flow (e.g. Beckmann et al., 1994; Biastoch and Krauss, 1999); T_3 is the transfer from EAPE to EKE ($P_e \rightarrow K_e$) through the vertical motion of water parcels with anomalous densities compared with the waters in the ambient; and T_4 is the conversion of MKE to EKE ($K_m \rightarrow K_e$) by the work of Reynolds stresses against the mean shear, which, if it is positive, indicates the occurrence of barotropic instability. Comparisons of energy conversion terms between the southern and northern sectors are presented in Fig. 11. We will identify the possible cause for the larger MKE and EAPE in the southern sector of the eddy (Fig. 8).

For the T_1 term, there was a transfer from MKE to MAPE in the northern sector of the eddy, while opposite energy transfers occurred for the southern sector. Weaker vertical displacement of the isopycnals (Fig. 5), due to smaller vertical motion, converted the MAPE to MKE and formed a larger value of MKE there. Similarly, the energy was transferred from MAPE to EAPE (term T_2) in the upper layers of the southern sector, which implied the

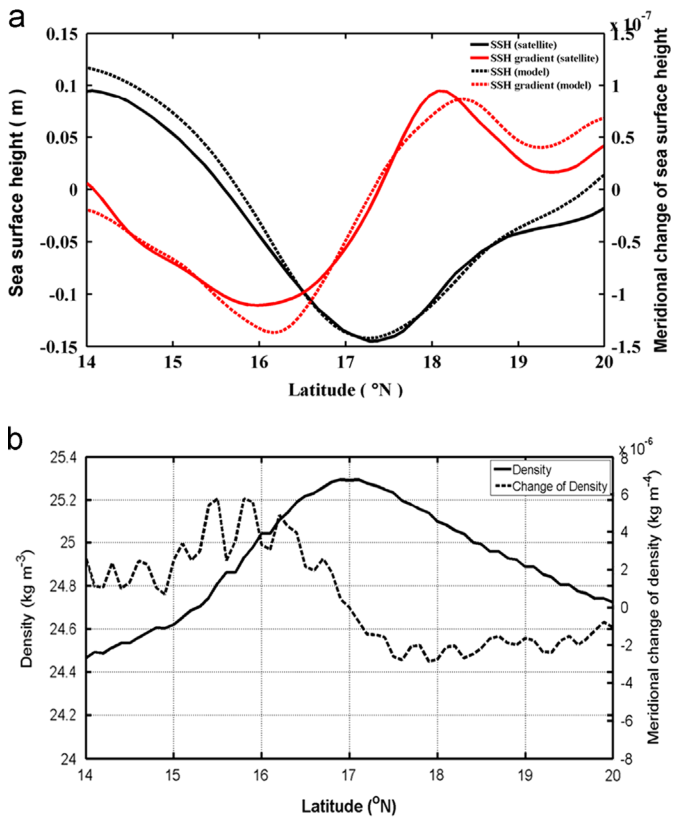

Fig. 10. (a) Sea surface height anomaly and meridional change of sea surface height and density in the upper 200 m across the eddy along 118.0°E in model results and satellite observations, and (b) mean density and meridional change of density in the upper 200 m across the eddy along 118.0°E in model results. Density is represented by the density anomaly (=density − 1000) with units of kg m^{-3}.

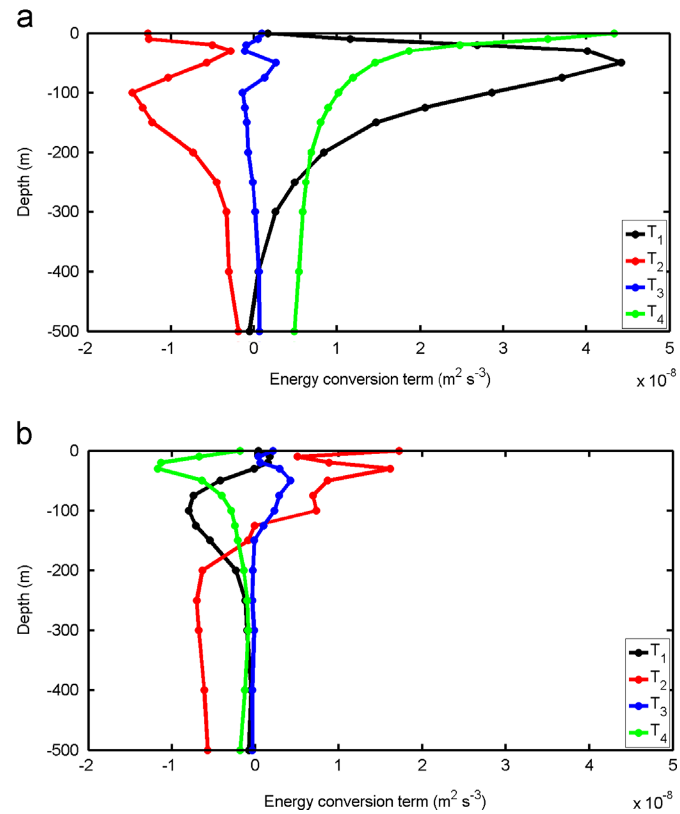

Fig. 11. Comparison of energy conversion terms between (a) the northern and (b) the southern sector of the eddy. The values on the southern sector of the eddy are averaged between 15 and 17°N and the values on the northern sector of the eddy are averaged between 17 and 19°N.

presence of baroclinic instability. In the north, the negative values of T_2 represented the opposite energy conversion. These positive/negative values of T_2 contributed to the higher EAPE in the southern sector compared to the north, and were consistent with the results obtained from analysis of momentum balance in Fig. 9.

For the T_3 term, energy conversions from EAPE to EKE existed for both the northern and southern sectors. Except near the pycnocline where the fluctuating buoyancy flux was relatively large (Fig. 5), the redistribution of energy from the EAPE to EKE was generally very small and had little contribution to the eddy asymmetry.

For the T_4 term, asymmetry also existed between the northern and southern sectors. In the north, direct conversion from MKE to EKE suggests that barotropic instability occurred. These barotropic energy conversions were considered to be mainly associated with the intrusions of large-scale forcing from the Pacific into the northern SCS along the northern coast of the Luzon Islands (e.g. Hu et al., 2000; Xue et al., 2004; Zheng et al., 2007). In the southern sector of the eddy, negative values of T_4 represented the energy transfer from the EKE to the MKE and contributed to more MKE and less EKE in the south than in the north (Fig. 8).

While stronger MKE in the south in the asymmetric WLE was directly linked to a stronger local current, we further investigated the source of larger EAPE in the south (Fig. 8b) using the time evolution of terms T_2 and T_4 and their associated EKE, and EAPE in the north and south sectors (Fig. 12). In the northern sector, the time evolution of the EKE was found to have a close relationship with the evolution of the T_4 term, suggesting that the EKE in the northern sector was mainly associated with the barotropic energy conversion from MKE to EKE. Zu et al. (2013) revealed that the Kuroshio intrusion branch could produce significant energy conversion from MKE to EKE. In the southern sector, the time evolution of the EAPE was found to have a close relationship with the evolution of the T_2 term, suggesting that the EAPE in the southern sector was mainly determined by the baroclinic energy conversion from MAPE to EAPE. The subsurface front between the WLE and the southern warm eddy provided a favorable condition for the occurrence of energy conversions from MAPE to EAPE. As a result, the southern sector of the WLE stored more EAPE; in contrast, more EKE was captured for the northern sector.

5. Summary

We analyzed the three-dimensional structure of the cold (cyclonic) WLE and the associated dynamic characteristics based on results obtained from a validated regional ocean model. The model is forced with high-frequency, time-dependent atmospheric forcing calculated from the NCEP reanalysis data and with real-time lateral fluxes from the Pacific Ocean Model. The model results have been well-validated in the previous studies and the comparisons of model results with available satellite observations in this study demonstrated that the model was able to reproduce the main features of the WLE.

This WLE was horizontally and vertically heterogeneous. Asymmetric structures existed in the circulation, vorticity, vertical motion and energy in the eddy. Stronger horizontal currents and vorticity occurred in the southern sector, where upwelling was strengthened. Asymmetric structures were also found in the energy distributions, with larger MKE and EAPE in the south and larger EKE in the north. While the WLE was formed by the vorticity imparted by local positive wind stress curl, the

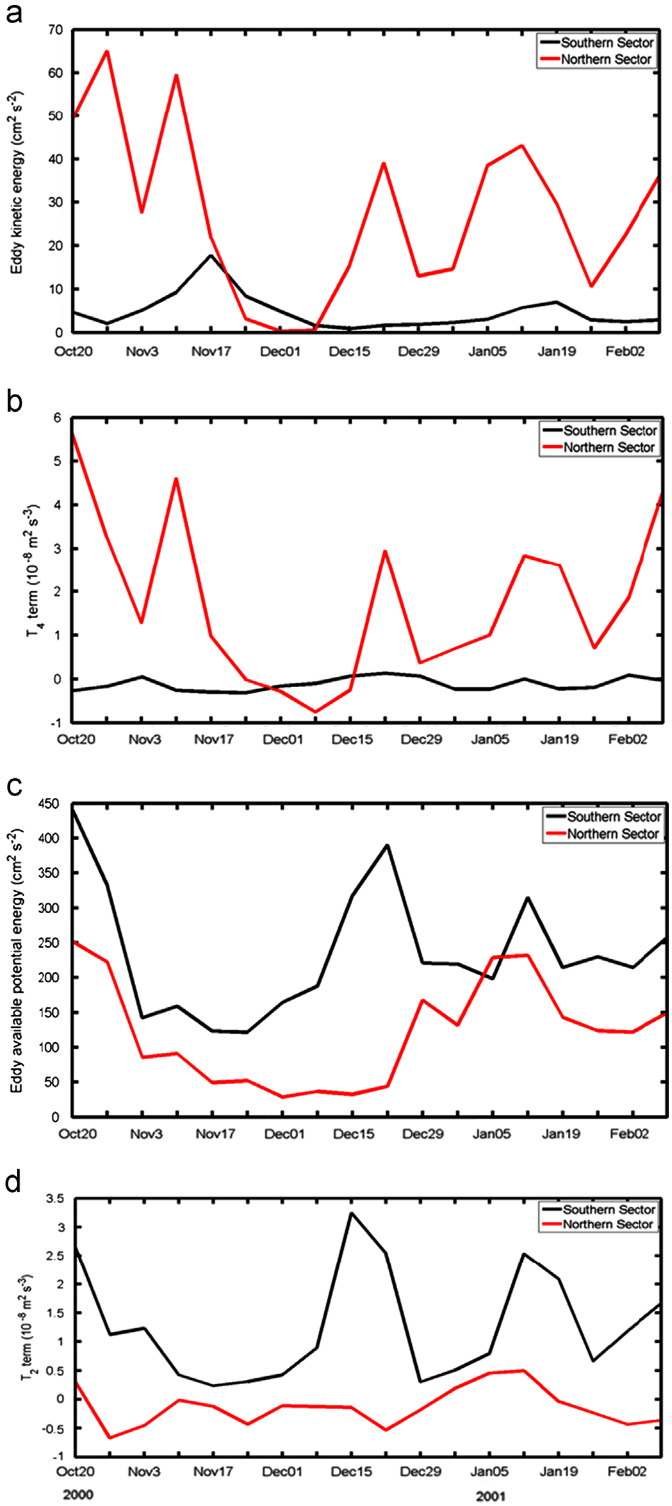

Fig. 12. The time evolution of (a) EKE, (b) T_4 term, (c) EAPE, and (d) T_2 term in the northern and southern sectors of the eddy from October 20, 2000 to February. 09, 2001.

asymmetric structure of the WLE was mainly attributed to the dynamics arising from an eddy dipole formed by a coexisting warm eddy to the south of the WLE.

Analyses of momentum balance were conducted to understand the dynamic characteristics in the asymmetric WLE and provide physical explanation for the asymmetry. The pressure difference between eddies in the dipole increased markedly meriodional BTPG and the eastward jet in the southern sector of the WLE. The strengthened positive vorticity in the jet intensified the WLE in the southern sector, but the negative vorticity of the jet weakened it farther south in the periphery, which, together with a subsurface front between the cold and warm eddy in the dipole, intensified and suppressed upwelling as well as cooling in the respective regions.

The WLE contained a core of high density water and set up a BCPG, which acted in the opposite way of the dominant BTPG and spun down the cyclonic circulation of the eddy. Large values of the BCPG attributed to the gradual weakening of the eddy below 200 m, with a much stronger weekening occurring in the southern sector near the subsurface front.

Analysis of the energy budget indicated that barotropic conversion from MKE to EKE occurred in the northern periphery and was likely associated with the intrusions of large-scale forcing from the Pacific (e.g., the Kuroshio intrusion) into the northern SCS. However, larger EAPE in the southern part was mainly caused by baroclinic conversion from MAPE to EAPE that was associated with frontal dynamics in the eddy dipole. The subsurface front provided a favorable condition for the baroclinic energy conversions from MAPE to EAPE. These barotropic and baroclinic energy conversions were consistent with the results found in the momentum balance and contributed to more EKE in the northern sector and more EAPE in the south.

It should be noted that the full picture of eddy dynamics is rather complex and largely unknown. Although we are far from providing a definitive explanation of the dynamics of the three-dimensional eddy, this study demonstrated the asymmetric characteristics of the WLE, and, by coherent analyses of momentum balance and energy budget, provided the physical explanation for the heterogeneity of the eddy. Recent research results (e.g., Wang et al., 2013) also suggested that intraseasonal variations in the SCS circulation are also significant. The temporal variations of the WLE on intraseasonal and other time scales are worthy to be analyzed in more details in future study.

Acknowledgments

This research was supported by the Key Project of the National Science Foundation of China (NSFC) (Grant no. 91228202), the National Key Basic Research Development Program (Grant no. 2014CB441501), and the Hong Kong's Research Grant Council under Project GRF601009. The authors are grateful for the data processing by Anson Cheung and Rong Zhang. The authors thank the anonymous reviewers for their comments and suggestions that have helped to improve our manuscript.

References

Babu, M.T., Kumar, S.P., Rao, D.P., 1991. A subsurface cyclonic eddy in the Bay of Bengal. J. Mar. Res. 49, 403–410.
Badin, G., Williams, R.G., Holt, J.T., Fernand, L.J., 2009. Are mesoscale eddies in shelf seas formed by baroclinic instability of tidal fronts? J. Geophys. Res. 114, C10021, http://dx.doi.org/10.1029/2009JC005340.
Beckmann, A., Boning, C.W., Brugge, B., Stammer, D., 1994. On the generation and role of eddy variability in the central North Atlantic Ocean. J. Geophys. Res. 99 (10) (20, 381–20, 391).
Biastoch, A., Krauss, W., 1999. The Role of mesoscale eddies in the source regions of the Agulhas Current. J. Phys. Oceanogr. 29, 2303–2317.
Blumberg, A.F., Mellor, G.L., 1987. A description of a three dimensional coastal ocean circulation model. In: Heap, N. (Ed.), Three-Dimensional Coastal Ocean Models, 4. AGU, Washington, D.C., p. 208.
Boning, C.W., Budich, R.G., 1992. Eddy dynamics in a primitive equation model: Sensitivity to horizontal resolution and friction. J. Phys. Oceanogr. 22, 361–381.
Brown, J.N., Fedorov, A.V., 2010. How much energy is transferred from winds to the thermocline on ENSO time scales? J. Clim. 23, 1563–1579.
Campos, E.J.D., Velhote, D., da Silveria, I.C.A., 2000. Shelf break upwelling driven by Brazil current cyclonic meanders. Geophys. Res. Lett., 27, pp. 751–754.

Chaigneau, A., Le Texier, M., Eldin, G., Grados, C., Pizarro, O., 2011. Vertical structure of mesoscale eddies in the eastern South Pacific Ocean: a composite analysis from altimetry and Argo profiling floats. J. Geophys. Res. 116, C11025, http://dx.doi.org/10.1029/2011JC007134.

Chelton, D., Schlax, M., Samelson, R., de Szoeke, R., 2007. Global observations of large oceanic eddies. Geophys. Res. Lett., 34, http://dx.doi.org/10.1029/2207GL03081267.

Chelton, D., Gaube, P., Schlax, M.G., Early, J.J., Samelson, R.M., 2011a. The influence of nonlinear mesoscale eddies on near-surface oceanic chlorophyll. Science 334, 328–332.

Chelton, D., Schlax, M., Samelson, R., 2011b. Global observations of nonlinear mesoscale eddies. Prog. Oceanogr. 91, 67–216.

Curchitser, E.N., Haidvogel, D.B., Hermann, A.J., Dobbins, E.L., Powell, T.M., Kaplan, A., 2005. Multi-scale modeling of the North Pacific Ocean: assessment and analysis of simulated basin-scale variability. J. Geophys. Res., 110, http://dx.doi.org/10.1029/2005JC002902.

Dong, C., Lin, X., Liu, Y., Nencioli, F., Chao, Y., Guan, Y., Chen, D., Dickey, T., McWilliams, J.C., 2012. Three-dimensional oceanic eddy analysis in the Southern California Bight from a numerical product. J. Geophys. Res. 117C00H14http://dxdoi.org/10.1029/2011JC007354.

Flament, P.J., Kennan, S.C., Knox, R.A., Niiler, P.P., Berstein, R.L., 1996. The three-dimensional structure of an upper ocean vortex in the tropical Pacific Ocean. Nature 383, 610–613.

Gan, J.P., Allen, J.S., 2005a. On open boundary conditions in a limited-area coastal model off Oregon. Part 1: response to idealized wind forcing. Ocean Model. 8, 113–115, http://dx.doi.org/10.1016/j.ocemod2003.12.006.

Gan, J., Allen, J.S., 2005b. Modeling upwelling circulation off the Oregon coast. J. Geophys. Res., 110, http://dx.doi.org/10.1029/2004JC002692.

Gan, J.P., Li, H., Curchitser, E.N., Haidvogel, D.B., 2006. Modeling South China Sea circulation: response to seasonal forcing regimes. J. Geophys. Res., 111, http://dx.doi.org/10.1029/2005JC003298.

Gan, J.P., Qu, T.D., 2008. Coastal jet separation and associated flow variability in the southwest South China Sea. Deep Sea Res. Part I 55, 1–19, http://dx.doi.org/10.1016/j.dsr.2007.09.008.

Gan, J.P., Ho, H., 2008. Identification of spatial variability and eddies in the circulation of the South China Sea. In: Gan, J. (Ed.), Advances in Geosciences, Ocean Science, 12. World Scientific, Singapore, pp. 243–260.

Gill, A.E., 1982. Atmosphere-Ocean Dynamics. Academic Press, California p. 662.

Hoskins, B.J., Bretherton, F.P., 1972. Atmospheric frontogenesis models: mathematical formulation and solution. J. Atmos. Sci. 29 (6439), 11–37.

Hu, J., Kawamura, H., Hongi, H., Qi, Y., 2000. A review on the currents in the South China Sea: Seasonal circulation, South China Sea Warm Current and Kuroshio intrusion. J. Oceanogr. 56, 607–624.

Hu, J., Gan, J., Sun, Z., Zhu, J., Dai, M., 2011. Observed three dimensional structure of a cold eddy in the southwestern South China Sea. J. Geophys. Res. 116, C05016, http://dx.doi.org/10.1029/2010JC006810.

Isern-Fontanet, J., Font, J., Garcia-Ladona, E., Emelianov, M., Millot, C., Taupier-Letage, I., 2004. Spatial structure of anticyclonic eddies in the Algerian basin (Mediterranean Sea) analyzed using the Okubo–Weiss parameter. Deep-Sea Res. II 51, 3009–3028.

Johannessen, J.A., Svendsen, E., Sandven, S., Johannessen, O.M., Lyger, K., 1989. Three-dimensional structure of mesoscale eddies in the Norwegian coastal current. J. Phys. Oceanogr. 19, 3–19.

Kawaguchi, Y., Itoh, M., Nishino, S., 2012. Detailed survey of a large baroclinic eddy with extremely high temperatures in the Western Canada basin. Deep-Sea Res. I 66, 90–102.

Lee, T.N., Yoder, J.A., Atkinson, L.P., 1991. Gulf stream frontal eddy influence on productivity of the southeast U.S. continental shelf. J. Geophys. Res. 96, 22191–22205.

Liu, Q., Kaneko, A., Su, J., 2008. Recent progress in studies of the South China Sea circulation. J. Oceanogr. 56, 607–624.

Lorenz, E.N., 1955. Available potential energy and the maintenance of the general circulation. Tellus 7, 157–167.

Martin, M.C., Villanoy, C.L., 2007. Sea surface variability of upwelling area northwest of Luzon, Philippines, Dynamic Planet. Springer, Berlin Heidelberg, pp. 84–87.

Mahadevan, A., Tandon, A., 2006. An analysis of mechanisms for submesoscale vertical motion at ocean fronts. Ocean Model. 14, 241–256.

McWilliams, J.C., 1985. Sub-mesoscale, coherent vortices in the ocean. Rev. Geophys. 23, 165–182, http://dx.doi.org/10.1029/RG023i002p00165.

McWilliams, J.C., 2008. The nature and consequences of oceanic eddies. In: Hecht, M.W., Hasumi, H. (Eds.), Ocean Modeling in an Eddying Regime, Geophysical Monograph Series, 177. AGU, Washington, D.C., pp. 5–15, http://dx.doi.org/10.1029/177GM03.

McGillicuddy, D.J., Robinson, A.R., Siegel, D.A., Jannasch, H.W., Johnson, R., Dickey, T. D., McNeil, J., Michaels, A.F., Knap, A.H., 1998. Influence of mesoscale eddies on new production in the Sargasso Sea. Nature 394, 263–266.

McGillicuddy, D.J., et al., 2007. Eddy/wind interactions stimulate extraordinary Mid-ocean plankton blooms. Science 316, 1021–1026.

Metzger, E.J., 2003. Upper ocean sensitivity to wind forcing in the South China Sea. J. Oceanogr. 59, 783–798.

Oke, P.R., Griffin, D.A., 2011. The cold-core eddy and strong upwelling off the coast of New South Wales in early 2007. Deep-Sea Res. II 58, 574–591.

Oort, A.H., Ascher, S.C., Levitus, S., Peixoto, J.P., 1989. New estimates of the available potential energy in the World Ocean. J. Geophys. Res. 94, 3187–3200.

Osgood, K.E., Bane, J.M., Dewar, W.K., 1987. Vertical velocities and dynamical balances in Gulf stream meanders. J. Geophys. Res. 92, 13029–13040.

Qu, T., 2000. Upper-layer circulation in the South China Sea. J. Phys. Oceanogr. 30, 1450–1460.

Soong, Y.S., Hu, J.H., Ho, C.R., 1995. Cold-core eddy detected in the South China Sea. EOS Trans. 76 (35), 345–347.

Shaw, P.T., Chao, S.Y., Fu, L., 1999. Sea surface height variations in the South China Sea from satellite altimetry. Oceanol. Acta 22, 1–17.

Shaw, P.T., Chao, S.Y., Liu, K.K., Pai, S.-C., Liu, C.T., 1996. Winter upwelling off Luzon in the northeastern South China Sea. J. Geophys. Res. 101, 16435–16448.

Tabata, S., 1982. The anticyclonic, baroclinic eddy off Sitka, Alaska, in the northeast Pacific Ocean. J. Phys. Oceanogr. 12, 1260–1282.

Udarbe-Walker, M.J., Villanoy, C.L., 2001. Structure of potential upwelling in the Philippines. Deep-Sea Res. I 48, 1499–1518.

Wang, G., Chen, D., Su, J.L., 2008. Winter eddy genesis in the eastern South China Sea due to orographic wind jets. J. Phys. Oceanogr. 38, 726–732, http://dx.doi.org/10.1175/2007JPO3868.1.

Wang, G., Ling, Z., Wu, R., Chen, C., 2013. Impacts of the Madden–Julian oscillation on the summer South China Sea ocean circulation and temperature. J. Climate 26, 8084–8096.

Xue, H., Chai, F., Pettigrew, N.R., Xu, D., Shi, M., Xu, J., 2004. Kuroshio Intrusion and the circulation in the South China Sea. J. Geophys. Res. 109, C02017, http://dx.doi.org/10.1029/2002JC001724.

Yang, H., Liu, Q., 2003. Forced Rossby wave in the Northern South China Sea. Deep-Sea Res. I 50, 917–926.

Yang, G., Wang, F., Li, Y., Lin, P., 2013. Mesoscale eddies in the northwestern subtropical Pacific Ocean: statistical characteristics and three-dimensional structures. J. Geophys. Res. 118, 1–20.

Zhang, Z., Y. Zhang, W. Wang, and R.X. Huang, 2013. Universal structure of mesoscale eddies in the ocean. Geophys. Res. Lett., http://dx.doi.org/10.1002/grl.50736.

Zheng, Z.W., Ho, C.R., Kuo, N.J., 2007. Mechanism of weakening of west Luzon eddy during La Nina years. Geophys. Res. Lett. 34, http://dx.doi.org/10.1029/2007GL030058.

Zu, T., Wang, D., Yan, C., Belkin, I., Zhuang, W., Chen, J., 2013. Evolution of an anticyclonic eddy southwest of Taiwan. Ocean Dyn. 63, 519–531.